Journal Pre-proof

Automated extraction of *in situ* contact angles from micro-computed tomography images of porous media

Anelechi Ibekwe, Dubravka Pokrajac, Yukie Tanino

PII: S0098-3004(18)30505-3
DOI: https://doi.org/10.1016/j.cageo.2020.104425
Reference: CAGEO 104425

To appear in: *Computers and Geosciences*

Received date : 28 May 2018
Revised date : 29 October 2019
Accepted date : 29 January 2020

Please cite this article as: A. Ibekwe, D. Pokrajac and Y. Tanino, Automated extraction of *in situ* contact angles from micro-computed tomography images of porous media. *Computers and Geosciences* (2020), doi: https://doi.org/10.1016/j.cageo.2020.104425.

Automated extraction of *in situ* contact angles from micro-computed tomography images of porous media

Anelechi Ibekwe*, Dubravka Pokrajac, Yukie Tanino

School of Engineering, University of Aberdeen, Aberdeen AB24 3UE, Scotland, United Kingdom

Abstract

We present a simple and robust algorithm for the automated measurement of *in situ* contact angles from segmented micro-computed tomography images of immiscible fluid pairs in porous media and 2D slices of them. The algorithm comprises three steps: identification of contact points, an initial coarse estimate of contact angle, and its refinement. To obtain the coarse estimate we identify the vectors which point into the wetting phase and are also normal to the fluid/fluid and fluid/solid surfaces within the vicinity of each contact point. The coarse estimate is subsequently refined by fitting planes across fluid/fluid and fluid/solid surfaces to obtain the final estimate of contact angle. The algorithm was applied to a packed bed of glass spheres using air/water as the fluid pairs. A wide distribution of contact angles spanning the full range of possible values was measured for both the 2D and 3D cases. The distributions are skewed towards their respective means and are longer-tailed compared to a Gaussian distribution. The mean contact angles were found to be approximately $65 \pm 21°$, which is significantly larger than bulk contact angles of $35 \pm 3°$ measured on a flat glass substrate using identical test fluids. The disagreement suggests that bulk contact angles can dramatically underestimate *in situ* contact angles even in the simplest porous media.

Keywords: `contact angle`, `wettability`, `micro-CT`, `tomography`, `multiphase flow`, `pore scale imaging`

1. Introduction

Wettability of a fluid/fluid/porous medium system is typically characterized by the contact angle that the fluids make on a mineralogically representative, polished, flat substrate. Contact angle measurements are

*Corresponding author

Email address: `anelechi.ibekwe@abdn.ac.uk` (Anelechi Ibekwe)

[1]Authorship statement: YT and DP conceived the research. DP conceived the algorithm. All authors designed the experiment. AI and DP acquired the data and implemented the algorithm. AI wrote the manuscript with input from all authors. All authors critically reviewed the manuscript.

usually carried out on such substrates using the traditional sessile drop [1–4] and captive bubble techniques [5–8] - and reported as single values for either water-advancing or water-receding contact angles. However, grain surfaces within natural porous media such as rock and soil are neither flat nor smooth, and values on flat, polished surfaces do not account for the geometrical complexity of the pore structure or the composition and lithological complexity of the grains [9–11]. Factors such as grain roughness [10, 12] and pore- and sub-pore scale heterogeneity in mineralogy within the porous medium [9, 13] are believed to influence contact angle values at the pore scale thereby resulting in a distribution of contact angles even within a geometrically uniform porous medium.

Advances in X-ray micro-computed tomography (micro-CT) have made it possible to map the three-dimensional pore structure of a porous material, hence providing information on size, shape, and continuity of the pore spaces [14–18]. Furthermore, it is now possible to conduct multiphase displacement tests as well as analyse *in situ* 3D distributions of multiple phases in porous media under varying conditions of pressure, temperature, and salinity [19–24]. This has prompted recent contact angle measurements at the pore scale of which the pioneering work was carried out by Andrew et al. [25], who measured *in situ* contact angles at reservoir conditions of 10 MPa and 50 °C for a supercritical CO_2/brine/carbonate system. Raw 2D images were positioned perpendicular to the three-phase contact lines, and vectors tangential to the fluid/fluid and fluid/solid surfaces were manually traced. Although this manual approach has subsequently been applied to bead packs and sand packs [26], micromodels [27], sandstones [28–31], and carbonates [32, 33], it is time consuming and may introduce significant errors due to its subjective nature.

Klise et al. [34] were the first to develop an algorithm for local contact angle measurements by fitting planes to the fluid/fluid and fluid/solid surfaces. Their method was applied to bead packs under both water-wet and mixed-wet conditions; more recently, the method has been applied to sandstone cores [31]. In their method, the fluid/fluid and fluid/solid interfaces were depicted as wetting phase voxels that share a face with the fluid and solid phases, respectively, wherefore contact points coincided with the interface points. The method developed by Andrew et al. [25] has since been automated by Scanziani et al. [35], who measured *in situ* contact angles in both water-wet and mixed-wet Ketton limestone. Their approach was based on the physical constraint of constant curvature of the fluid/fluid interface which enabled the authors to infer the actual location of the three-phase contact by fitting a circle to the fluid/fluid interface and a line to the grain surface. Most recently, AlRatrout et al. [36] measured *in situ* contact angles by applying various smoothing procedures to the voxelized pore scale images before computing the vectors perpendicular to the fluid/fluid and fluid/solid surfaces. Like Scanziani et al. [35], their approach was also based on the

physical constraint of uniform fluid/fluid curvature. The methods of Scanziani et al. [35] and Al Ratrout et al. [36] have since been applied on carbonate core samples (see Refs. [37] and [33, 38, 39], respectively).

Although the existing automated algorithms provide reliable estimates of contact angles, they are however either complex in their application due to the imposition of a spherical fluid/fluid curvature (AlRatrout et al. [36] and Scanziani et al. [35]), or prone to errors due to the depiction of an interface as one-voxel thick (Klise et al. [34]). In this study, we provide a simple algorithm that reliably extracts *in situ* contact angles. The algorithm can measure *in situ* contact angles regardless of the configuration of the pore space and geometry of the local fluid/fluid curvature. The algorithm is described in Section 2 and results of the validation and sensitivity studies are presented in Section 3. Finally, the algorithm is applied to an air/water/glass tomogram in Section 4.

2. Algorithm for contact angle extraction

The input data for the algorithm are segmented pore space images. A stack of slices forms a 3D data set.

2.1. 2D Algorithm

Here we present two stages for the extraction of *in situ* contact angles from pore space images of immiscible fluids in a porous medium: a coarse (intermediate) and a fine estimate of contact angles. The latter is a refinement of the former - and was implemented to enhance the accuracy of the contact angle extraction.

Coarse estimate

A uniform mesh covers the image wherein each pixel (or voxel) is assigned a single phase (wetting, non-wetting, and solid phases), denoted with W, N and S, respectively. The mesh nodes are the points where the edges of the adjacent pixels meet. Their numbering is shown in Fig. 1.

An interface is here defined as the edge between any two pixels of different phases. Furthermore, the edge between a solid and a wetting phase is a Wetting/Solid interface (WS) and that between a Non-wetting and a wetting phase is a Wetting/Non-wetting (WN) interface. In the present work, we are not particularly interested in the Solid/Non-wetting interface.

Definition of an X-point and normal vector for a node in 2D

For the 2D algorithm, we refer to the centre of each WS or WN interface as an "X-point". The locations of potential X-points next to a node (*ix, iy*) are in the middle of the four edges meeting at *ix, iy*. They are

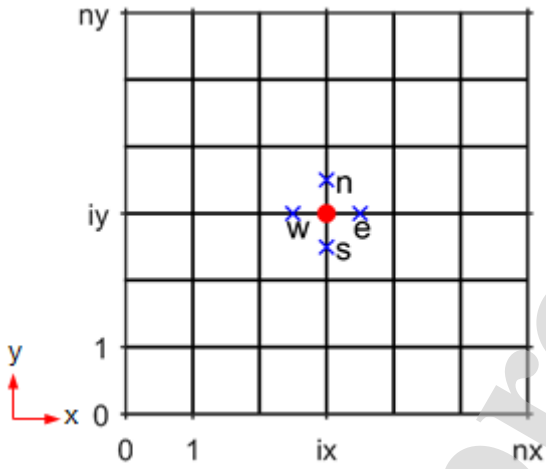

Fig. 1: A 2D computational node (ix, iy) showing adjacent potential X-points

denoted with e, w, n, s (east, west, north, south) as shown in Fig. 1. A potential X-point becomes an actual X-point if it is located at either WS or WN interface. The example of two actual X-points with respect to a node is shown in Fig. 2a. A normal unit vector $\boldsymbol{n}$ which points into the wetting phase is defined at each X-point. The algorithm computes and stores the normal vector components for X-points at the east, west, north and south locations around each node.

Contact point extraction and normal vector collation within the contact point neighbourhood

Contact points are the nodes where the solid, non-wetting and wetting phases meet. They are extracted by finding all nodes that are adjacent to at least one X-point with a WS normal vector and another one with a WN normal vector. For each contact point, a search algorithm extracts all connected WS edges and the associated X-points and normal vectors $\boldsymbol{n}_i$ within a search radius R_1 (Fig. 2b). Analogous search is carried out for WN interfaces. The average of all WS normal vectors collated for each contact point is computed as:

$$\begin{aligned} {n_x}^{\mathrm{WS}} &= \frac{1}{N}\sum_{i=1}^{N} n_{xi}, \\ {n_y}^{\mathrm{WS}} &= \frac{1}{N}\sum_{i=1}^{N} n_{yi}, \end{aligned} \tag{1}$$

where $(n_x^{\mathrm{WS}}, n_y^{\mathrm{WS}})$ is the average normal vector of the WS interface; N is the number of WS normal vectors within the specified search radius around contact point; n_{xi} and n_{yi} are the x and y components, respectively, of the normal vectors within the search radius. The average normal vectors of the WN interfaces

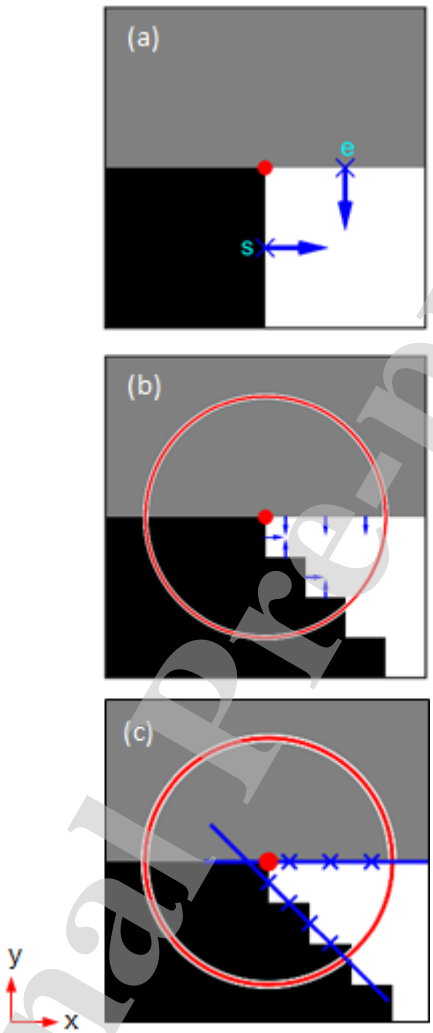

Fig. 2: Part of a segmented 2D image, with black, white, and grey, representing non-wetting, wetting, and solid pixels, respectively. A contact point is shown as the red dot. (a) Location of two actual X-points with respect to a node in 2D. (b) Normal vector collation within a contact point neighbourhood. (c) 2D representation of the fine estimate. Circle represents the search radius (here 3 pixels). X-points are shown as blue × marks; s and e represent the south and east locations of the current node, respectively. Blue arrows depicts the WS and WN normal vectors pointing into the wetting phase while blue lines represents the WS and WN interfaces.

are calculated in analogous way.

Dividing the WS average normal vector by its modulus, yields the unit WS average normal vector:

$$\hat{\boldsymbol{n}}^{\mathrm{WS}} = \frac{\boldsymbol{n}^{\mathrm{WS}}}{|\boldsymbol{n}^{\mathrm{WS}}|} \tag{2}$$

The angle between the WS and WN interfaces, i.e. the contact angle, θ, is given by:

$$\theta = 180^{\circ} - \cos^{-1}(\hat{\boldsymbol{n}}^{\mathrm{WS}}.\hat{\boldsymbol{n}}^{\mathrm{WN}}), \tag{3}$$

where $\hat{\boldsymbol{n}}^{\mathrm{WS}}$ and $\hat{\boldsymbol{n}}^{\mathrm{WN}}$ are the estimated unit normal vectors of the WS and WN interfaces that meet at the contact point, respectively; $\cos^{-1}(\hat{\boldsymbol{n}}^{\mathrm{WS}}.\hat{\boldsymbol{n}}^{\mathrm{WN}})$ is the angle (in degrees) between the two normal vectors (in the range 0° to 180°).

Fine estimate

In this final step of the algorithm, lines are fitted to the connected X-points of each WS and WN interface. The fitting is based on minimizing the squared distance between the line and the points. The lines which make an angle with the x axis in the range $(-45^{\circ},\ 45^{\circ})$ or $(135^{\circ},\ 225^{\circ})$ are fitted as $y(x)$ whereas all others are fitted as $x(y)$. The correct normal directions (pointing into the wetting phase) of the fitted WS and WN lines are established by comparison with the corresponding average normal vectors of the coarse estimate. Fig. 2c shows an example of the fine estimate.

2.2. 3D Algorithm

To extend the algorithm to 3D, it is important to understand how each term used in the 2D is represented in 3D. An X-point in 3D is at the centre of a face rather than centre of an edge as in 2D (Fig. 3); an interface in 3D is a surface rather than a line; the three-phase contact in 3D is a contact line rather than a contact point (vertex). The contact line for a single voxel is represented by its midpoint (located at an edge-centre or a "node" in 2D), which is referred to as contact point.

Since a 3D geometry consists of a set of 2D slices (in yz, zx, and xy planes), the 3D algorithm for the fine estimate entails finding all X-points as well as their corresponding normal vectors within the vicinity R_1 of each contact point located in each 2D plane (i.e., repeating the 2D algorithm for each 2D plane). A second search is further implemented, this time with radius R_2, such that all contact points sitting on the same contact line are identified. A plane is then fitted, based on minimizing the squared distance of the

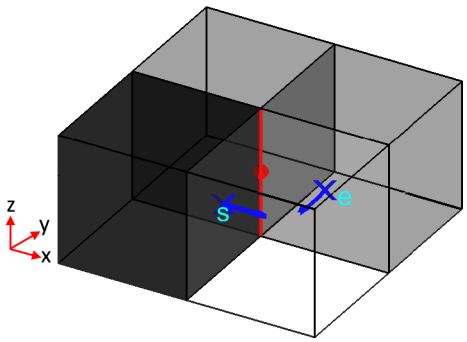

Fig. 3: Location of an X-point with respect to a node in 3D. Black, white, and grey represents non-wetting, wetting, and solid voxels, respectively. The three-phase contact line and its midpoint (contact point) are shown as red line and red dot, respectively. X-points are shown as blue $\times$ marks at the south and east locations of the contact line while blue arrows depict the WS and WN normal vectors.

fitting plane, through all adjacent contact points and their corresponding X-points. The fitting procedure is a 3D version of that already described for 2D.

For each contact point, a rough estimate of contact angle is found from the average WS and WN normal vectors of all X-points within the vicinity of the contact point, and the fine estimate is found from the WS and WN normal vectors of the fitted planes. Results of the sensitivity study carried out to determine the optimum combinations of R_1 and R_2 of the fine estimate are presented in Section 3. However, since there is no change in the procedure between the 2D and 3D versions of the coarse estimate, we adopt the same optimum R_1 for both cases.

3. Validation

3.1. Sensitivity to resolution

The proposed algorithm was validated using synthetic images of idealized geometries that intersect at known angles (Fig. 4). The synthetic image consists of a single circular (spherical in 3D) non-wetting phase droplet in contact with a solid surface and surrounded by the wetting phase [34, 35] as shown in Fig. 5. The WS interface is shifted from top to bottom to define the range of contact angles from 0-180°. At each WS interface shift for the 3D computation, contact points form a rim around the droplet. The algorithm computes the contact angles along the rim by implementing the methods described in Section 2. A pair of contact angles are obtained for each measurement (i.e. specified true angle) of the 2D computation, whereas

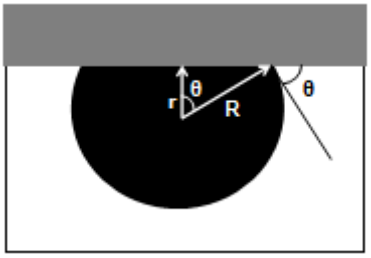

Fig. 4: Idealized geometry of contact angle formed between a non-wetting phase droplet (black) on a solid surface (grey), submerged in the wetting phase (white).

a set of values are obtained for the 3D cases. In the latter case, the extracted contacted angle for each measurement is equal to the mean value of all angles found along the contact rim.

Sensitivity to resolutions was studied by varying the number of pixels (or voxels) across the droplet diameter (Fig. 5). Specifically, the range of resolutions considered were 14-896 pixels/circle diameter in 2D and 14-112 voxels/sphere diameter in 3D. The search radius R_1 surrounding a contact point were also varied between 1-25% of the circle diameter (1-15% of the sphere diameter in 3D). Similarly, R_2 for the 3D case were also varied between 1-15 voxels around the contact point. True and extracted angles were compared by calculating the root mean square error (RMSE) for each resolution and search radius as:

$$\mathrm{RMSE} = \sqrt{\frac{1}{n}\sum_{i=1}^{n}\left(\theta_{\mathrm{i}} - \hat{\theta}_{\mathrm{i}}\right)^2}, \tag{4}$$

where n is the number of measurements, $\hat{\theta}_{\mathrm{i}}$ is the true contact angle, and θ_{i} is the i^{th} extracted contact angle.

Fig. 6 indicates that increasing the resolution results in lower RMSE values - thus yielding results that more closely approximate the true values. Also, a close inspection of Fig. 7 shows that for each resolution there is a critical (optimum) search radius required to achieve the best estimates of contact angles. The relationship between the optimum search radius and the resolution is such that the better the resolution, the smaller the percentage optimum search radius. Scatter plots (Fig. 8) of true versus extracted contact angles for both coarse and fine estimates at optimum search radius further highlights the impact of resolution on the contact angle measurements.

The results obtained for both 2D and 3D measurements at the optimum search radius are presented in Tables 1 and 2, respectively. Comparisons between 2D and 3D measurements of the fine estimate shows

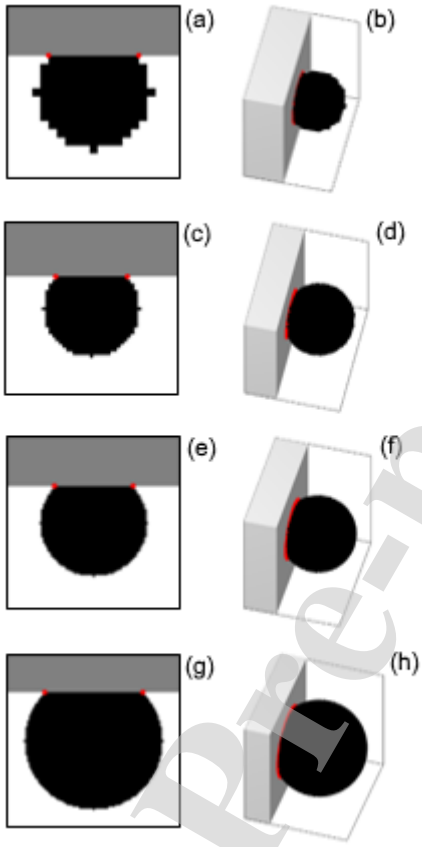

Fig. 5: 2D synthetic images at resolutions of (a) 14, (c) 28, (e) 56, and (g) 80 pixels/circle diameter, respectively. 3D synthetic images showing (b) 14, (d) 28, (f) 56, and (h) 80 voxels/sphere diameter, respectively. Black, white, and grey represents non-wetting, wetting, and solid phases, respectively. All images (a to h) are at 45° true contact angles. Contact points are shown in red.

Table 1: Results of sensitivity study for the 2D contact angle extraction at optimum R_1. For each resolution, RMSE is calculated over 10 measurements of $\hat{\theta}_i$.

Resolution	Coarse estimate		Fine estimate	
[pixels/circle diameter]	Optimum R_1 [pixels]	RMSE [°]	Optimum R_1 [pixels]	RMSE [°]
14	1.50	27.5	2.50	27.4
28	3.50	16.9	2.50	15.0
56	5.00	11.5	5.00	10.7
80	5.00	6.81	5.00	4.50
112	6.00	5.86	7.00	5.22
224	6.00	2.77	8.00	1.74
448	11.5	1.88	9.00	1.16
640	11.5	2.21	13.5	1.32
896	11.5	1.15	14.5	0.47

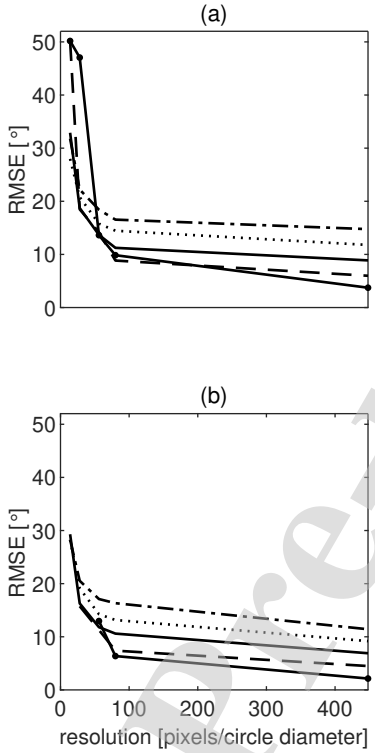

Fig. 6: RMSE versus resolution for (a) coarse and (b) fine estimate of the 2D algorithm. Search radius of 5, 10, 15, 20 and 25 % circle diameter are represented as solid line with dot, dashed, solid, dotted, and dashed-dotted lines, respectively.

Table 2: Results of sensitivity study for the 3D contact angle extraction at optimum combination of R_1 and R_2 of the fine estimate. For each resolution, RMSE is calculated over 10 measurements of $\hat{\theta}_i$.

Resolution [voxels/sphere diameter]	Optimum R_1 [voxels]	Optimum R_2 [voxels]	RMSE [°]
14	1.50	5.00	24.0
28	3.00	6.00	12.9
56	4.00	7.00	8.21
80	3.00	10.0	4.71
112	4.00	13.0	3.89

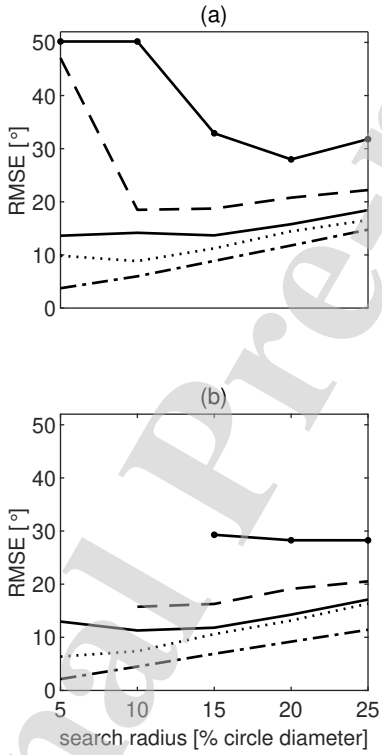

Fig. 7: RMSE versus search radius for (a) coarse and (b) fine estimate of the 2D algorithm. Resolution of 14, 28, 56, 80 and 448 pixels/circle diameter are represented as solid line with dot, dashed, solid, dotted, and dashed-dotted lines, respectively.

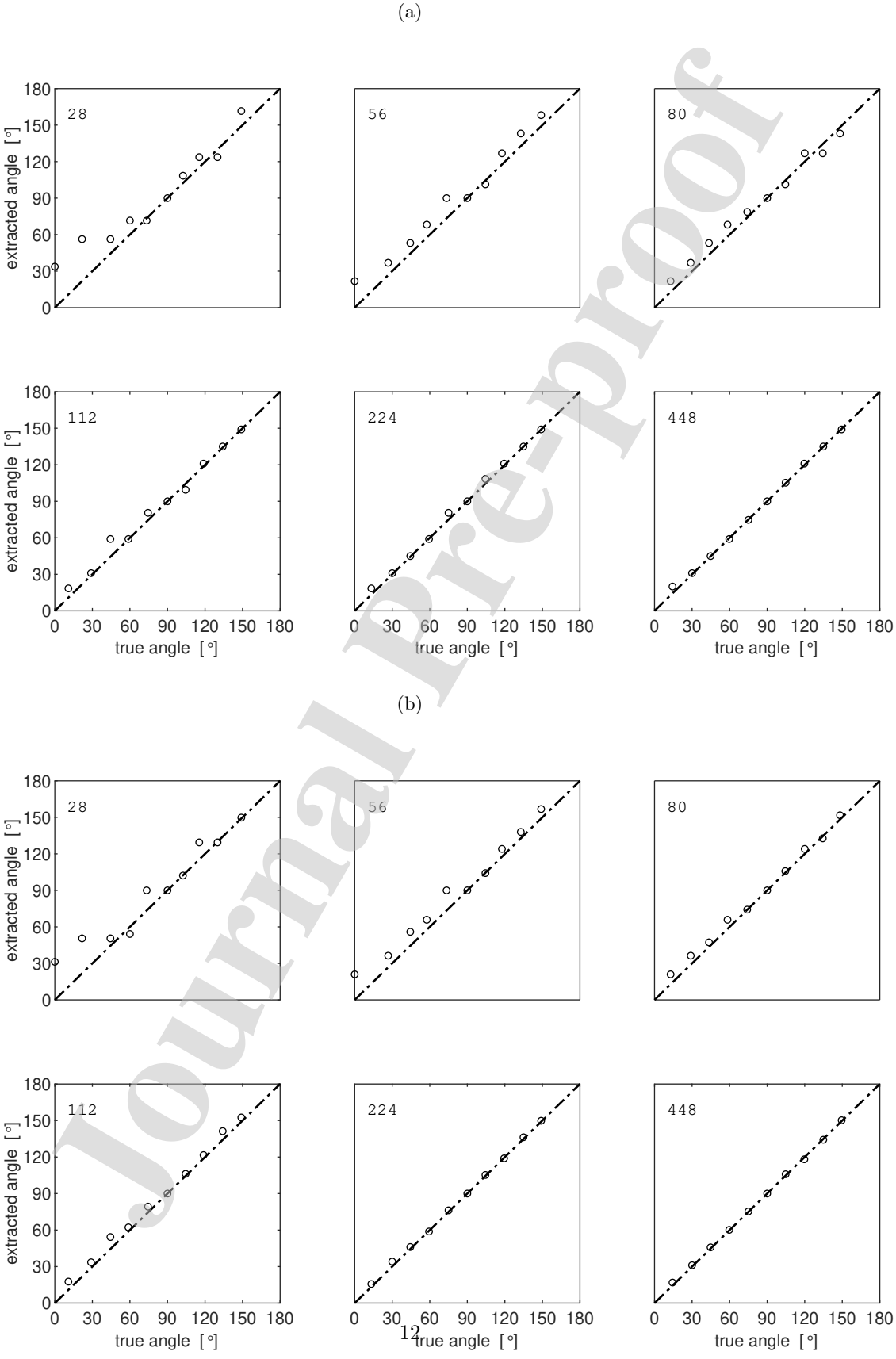

Fig. 8: Extracted contact angle as a function of the true contact angle for (a) coarse and (b) fine estimate at optimum search radius and resolutions of 28, 56, 80, 112, 224, and 448 pixels/circle diameter.

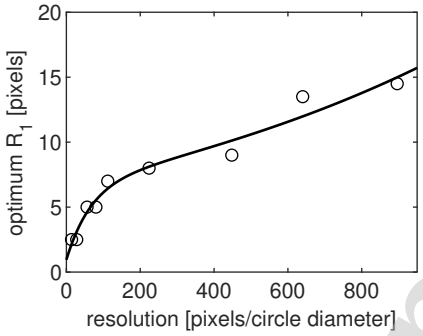

Fig. 9: Correlation between resolution and optimum search radius R_1 of the 2D algorithm. Solid line is a guide to the eye.

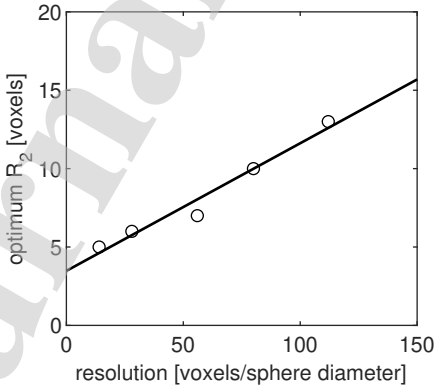

Fig. 10: Correlation between resolution and optimum search radius R_2 of the 3D algorithm. Solid line is a line of best-fit in the least-squares sense and is intended as a guide to the eye.

almost a consistent reduction in RMSE values. In addition, the fine estimate typically has better RMSE values compared to the coarse estimate. For the fine estimate, the relationship between R_1 and resolution is well described by a double exponential function (Fig. 9), while the relationship between R_2 and resolution is well described by a linear function (Fig. 10).

RMSE values obtained by Klise et al. [34] for resolutions of 14, 28, and 56 voxels/sphere diameter, are 13.2°, 7.3°, and 5.7°, respectively, whereas those obtained by Scanziani et al. [35] and AlRatrout et al. [36] are respectively 6.5°, 3.5°, 0.5° and 1.6°, 2.1°, 2.5°. The RMSE values of the fine estimate of the present algorithm are comparable to the results from Klise et al. for finer resolutions. It should be stated however that results from both Scanziani et al. and AlRatrout et al. were obtained after efforts were made to smooth the surfaces. In addition, their assumption of a spherical fluid/fluid curvature corresponds easily with the spherical non-wetting phase droplet employed in the synthetic image, thus making the validation biased towards the algorithms which make this assumption.

3.2. Comparison with the method of Scanziani et al. [35]

Contact angles were extracted from the segmented images of the oil ganglion SSa [40] acquired by Scanziani et al. [35] using our 3D (fine estimate) algorithm. SSa is a subset of a 2 μm scan acquired from a decane/brine/Ketton limestone system that has undergone a single drainage-waterflood cycle. The mean diameter of the grains surrounding the ganglion is ≈ 674 pixels. Accordingly, R_1 and R_2 were set to 14 and 56 voxels, respectively (Figs. 9 and 10).

Fig. 11 presents the contact angle distribution extracted using the present algorithm (black). The mean and and standard deviation are calculated as $56 \pm 12°$. This is larger than the static bulk n-decane/brine contact angle of $\theta_b = 29 \pm 5°$ measured previously on polished calcite [41]. This deviation is comparable to what was observed between *in situ* air/water/glass beadpack and bulk contact angle reported in Section 4.1. The deviation is attributed in part to the confinement imposed by the grain surface, which have been observed to elevate static air/liquid contact angles in glass capillaries by as much as 40° above their respective values on a flat substrate [42]. Superposed in Fig. 11 (blue) are angles evaluated by Scanziani et al. [35] using their algorithm. Their algorithm yields a distribution with comparable standard deviation, but with a mean that is 18° smaller than the present algorithm (Table 3). This difference may have resulted from the smoothing of the grain surface as implemented by Scanziani et al. [35] - which culminates in the removal of the voxelization artefacts. Nevertheless, Fig. 11 shows that the contact angle distribution from both methods are very similar; the distribution from the 3D fine estimate are shifted to the right, however, reflecting the

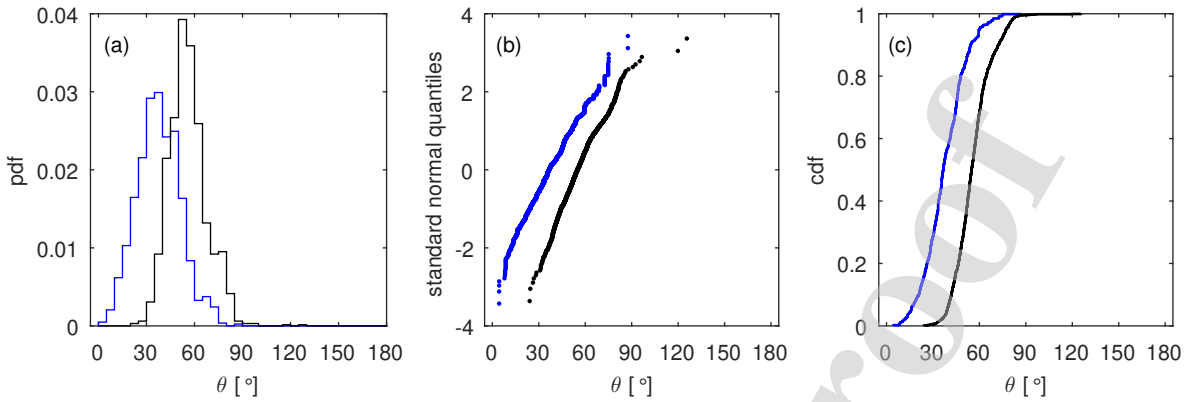

Fig. 11: The probability density function (a), standard normal quantiles (b), and cumulative distribution function (c) of measured contact angles from oil ganglion SSa in Scanziani et al. [35] (blue; actual values of extracted contact angles were provided by K. Singh, personal comm.) and the current method (black). Mean and standard deviations are reported in Table 3.

Table 3: Contact angle statistics from oil ganglion SSa in Scanziani et al. [35] compared with our automatic method. N_{cp} represents the number of contact point used in the calculation.

Parameter	Scanziani et al.	3D Fine
N_{cp}	1652	1304
Mean	37.7°	55.9°
Std. dev.	13.5°	11.6°

difference in the mean contact angle. Thus, in spite of the drawback highlighted herein, it is safe to say that the current method works on real rocks.

Interestingly, the number of contact points available for the calculation is reduced by 21% in the 3D Fine estimate (see Table 3). There are a number of reasons why this might be the case. For the current algorithm: (i) contact points with X-points which do not allow a complete evaluation of the search radius are deemed to likely be an artefact of segmentation and are thus discarded. In other words, there are not sufficient connected X-points within the search radius to evaluate the contact angle, (ii) contact points that are close by 1.5 voxels are invalidated, and (iii) contact points with more than one possible X-point from a given node are also invalidated.

4. Application

4.1. Materials

The porous medium used for applying our approach is a 38 mm-long, 21 mm-diameter column wet-packed with soda lime glass spheres (Mo-Sci Corporation, USA). The average diameter of the sphere is 966 ± 34 μm (standard deviation, 35 samples). To pack the column, the glass spheres were gradually introduced into a water-filled column while tapping the column constantly so as to achieve a close, random, and homogeneous packing. A valve at the bottom of the column was then opened to allow water to be drained and air to enter the medium from the top of the column. The drainage process was continued until equilibrium was attained. Scanning was performed 24 hrs from the time the drainage process began.

Static bulk contact angle measurements were carried out using a fully automated image capture system (Dataphysics OCA-20 Instruments GmbH, Germany). The test materials used were glass substrates (Agar scientific, UK) with air/water as the test fluids. Both the substrates and the microliter syringe were cleaned sequentially with toluene, propanol and water, and then air-dried. The same protocol was also applied in cleaning the glass spheres prior to packing. A mean contact angle of 35 ± 3° was obtained over 12 measurements - and a fresh substrate was used for each measurement.

4.2. Segmentation

Three dimensional tomograms at resolutions of 1.25 μm ($2000 \times 2000 \times 2000$ voxels) and 10 μm ($1000 \times 1000 \times 1000$ voxels) were acquired from the air/water/glass system using a Zeiss XRadia Versa 410 3D X-ray micro-CT scanner with a 140 kV/10 W X-rays source housed in the School of Engineering at University of Aberdeen. The raw 1.25 μm tomograms were segmented into air, water, and glass phases using the Trainable WEKA segmentation, which is a machine learning-based segmentation method [43]. A sample of the raw and segmented tomogram is shown in Fig. 12. To train a classifier, the Fast-random forest algorithm was implemented along with texture filters such as mean, variance and edges [33]. The raw 10 μm tomograms were first filtered with a $3 \times 3 \times 3$ kernel size median filter, then segmented into air, water, and glass phases with the seeded watershed algorithm using Avizo 9.0 software. The seeded watershed algorithm was implemented by first choosing grayscale intensity and gradient magnitude from the intensity histogram generated from the reconstructed tomograms. These were used as initial seed regions for each class (phase) - and the algorithm proceeded by growing the region boundaries in an iterative process wherefore voxels are assigned to their respective classes until convergence is achieved [44]. The porosity from the segmented 10 μm images was measured to be 35.6 ± 0.2% (standard deviation, 6 samples of size 10 mm^3 per sample).

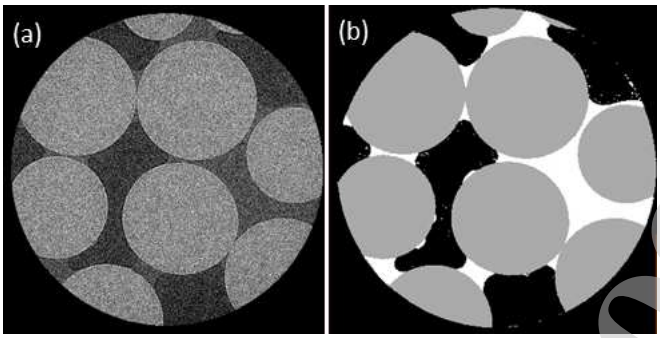

Fig. 12: Sample of the (a) raw and (b) segmented images of the 1.25 μm scan. Air, water, and solid phase are represented in the segmented image as black, white, and grey, respectively.

The algorithm was applied to the air/water/glass system described above. Resolutions of 1.25 and 10 μm/voxel correspond to 770 and 96 voxels/sphere diameter. Accordingly, we set the search radius R_1 for the 2D and 3D coarse estimates as 11.5 pixels and 11.5 voxels, respectively. For the fine estimate, R_1 was set as 13.5 pixels for the 2D measurement, while R_1 and R_2 for the 3D measurement were set as 14 and 56 voxels, respectively (Figs. 9 and 10). Three regions of interest (ROI) of 1280 $\times$ 1280 $\times$ 640 voxels centred at the vertical axis of the tomogram were selected for the 3D calculations. 2D contact angles were also extracted from the vertical slices of each ROI. Also, we set the search radius R_1 as 5 pixels for the 2D fine estimate of the 10 μm scan.

4.3. Results

4.3.1. Automatic contact angle estimates

The quantile of a probability distribution is the division of the dataset into intervals of equal probabilities. If θ_i is the sorted (in ascending order) data set, then the p^{th} sample quantile is given by

$$p_i = \frac{i - 0.5}{N}, \tag{5}$$

where N is the sample size; i is the rank of θ_i from 1 to N and p lies in the interval [0, 1]. The theoretical quantile (z-percentile) of a standard normal distribution is the inverse cumulative distribution function of the empirical (sample) quantiles. The standard normal quantile plot (i.e., z-percentile versus θ_i) provides a comparison between the empirical and theoretical quantiles.

The probability density function (pdf), quantile, and cumulative distribution function (cdf) of the extracted contact angles of the 1.25 μm scan are presented in Figs. 13 and 14 for fine estimates of the 2D and

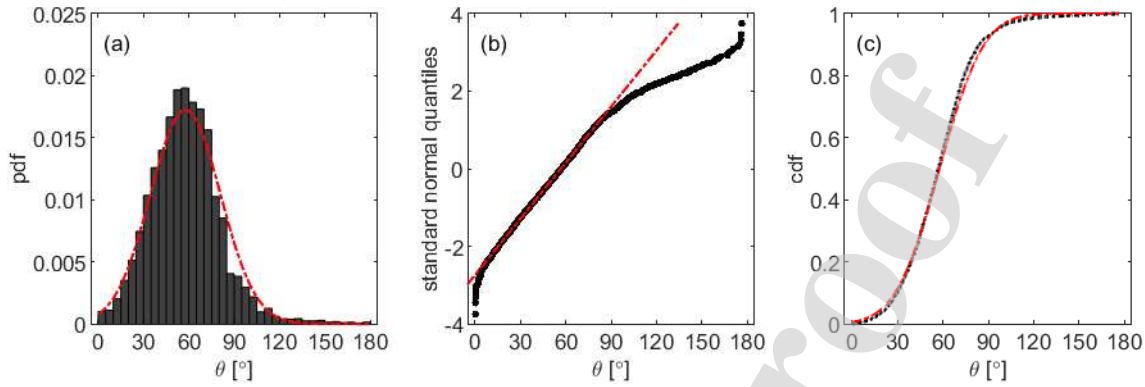

Fig. 13: The probability density function (a), standard normal quantiles (b), and cumulative distribution function (c) of measured 2D contact angles (black) and a Gaussian distribution with the same mean and standard deviation as the data (red dashed line). Mean and standard deviation are reported in Table 4 (ROI 1). Vertical arrow in (a) indicate bulk contact angle, $\theta_b = 35 \pm 3°$. The standard deviation of $\pm 3°$ is smaller than the marker size.

3D algorithms, respectively; superposed are standard normal distributions (red dashed) with a mean and standard deviation matched to the respective data. The results show that a wide distribution of contact angles is possible even for uniform glass spheres. The measured values are skewed towards their mean, but deviate at large ($\theta > 90°$) and small ($\theta < 30°$) angles. The observed distribution is longer-tailed compared to a Gaussian distribution: observed values are smaller than the z-percentile for a standard normal distribution at z > 1.5 and larger than the z-percentile at z < -2. The deviation is attributed to the density function decreasing gradually to zero in the tails [45]. The observed distribution differs from the truncated Gaussian distribution reported by Scanziani et al. [35] and the Gaussian distributions assumed by AlRatrout et al. [36] and Andrew et al. [25] in water-wet Ketton limestone, as well as the Gaussian distribution assumed by Tudek et al. [30] in Mount Simon sandstone.

The statistical data of the extracted contact angles are presented in Tables 4 and 5 for 2D and 3D calculations, respectively. The mean contact angles indicate that the system is water-wet (Tables 4, 5). This result agrees with median contact angle of 54.8° reported previously by Klise et al. [34] for kerosene/brine/glass-bead system. However, the result is significantly larger than bulk contact angles of $35 \pm 3°$ measured on a flat glass substrate using identical test fluids, and demonstrates that a single, bulk contact angle on a flat substrate does not fully characterize the wettability of a porous medium. The difference in the mean extracted contact angle between the 2D and 3D cases is 2.9° and 4.7° for the coarse and fine estimates,

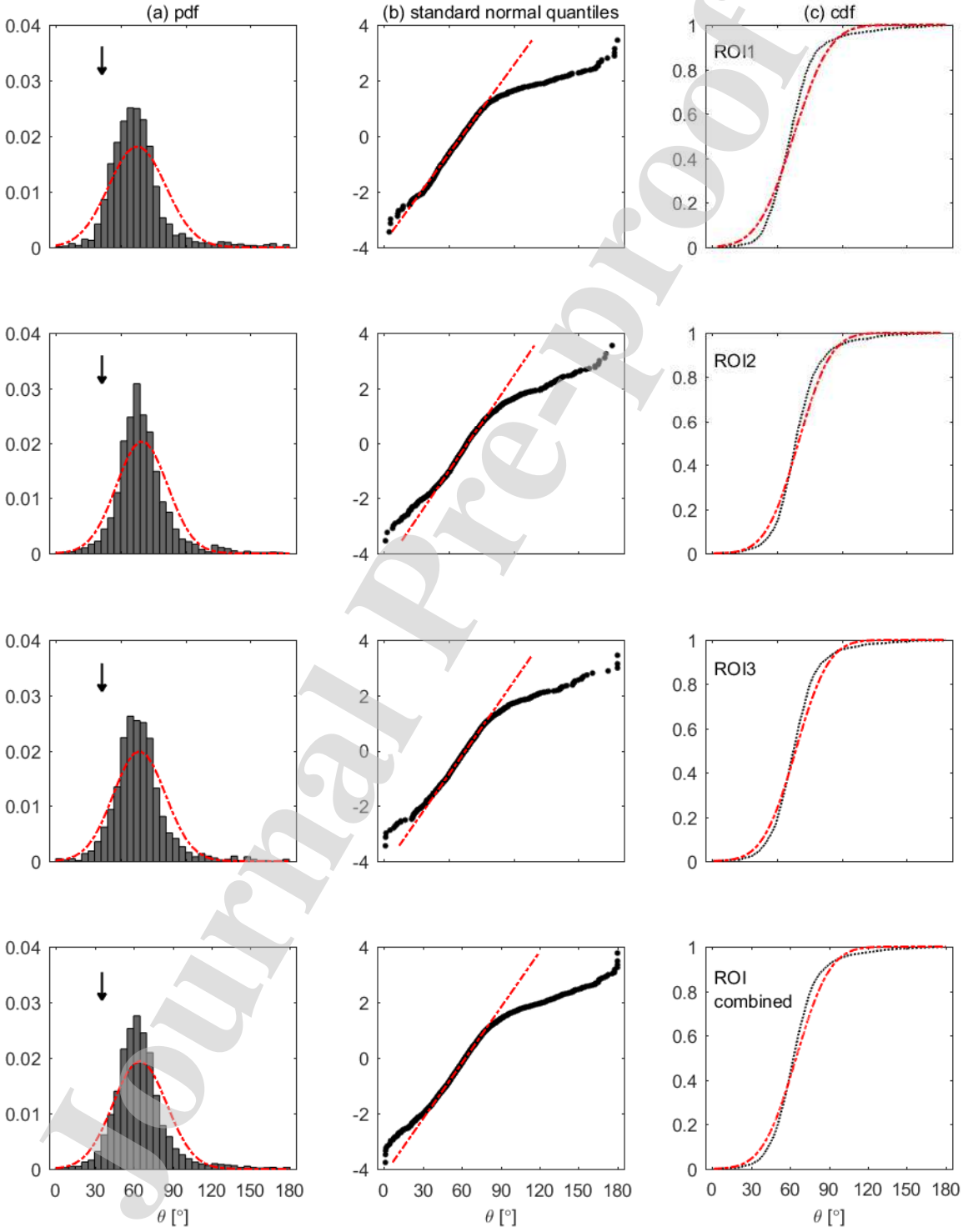

Fig. 14: The probability density function (a), standard normal quantiles (b), and cumulative distribution function (c) of measured 3D contact angles (black) and a Gaussian distribution with the same mean and standard deviation as the data (red dashed line). Mean and standard deviation are reported in Table 5. Vertical arrows in (a) indicate bulk contact angle, $\theta_b = 35 \pm 3°$. The standard deviation of $\pm 3°$ is smaller than the marker size.

Table 4: 2D contact angle statistics for the air/water/glass-bead system. Each slice is 1280 × 1280 pixels. N_{cp} represents the number of contact point used in the calculation.

Parameters	Coarse estimate			
	ROI 1	ROI 2	ROI 3	ROI combined
N_{cp}	6005	7815	5901	19721
Mean	63.7°	69.1°	62.8°	65.6°
Std. dev.	24.0°	22.0°	25.3°	23.8°
	Fine estimate			
N_{cp}	5578	7262	5449	18289
Mean	57.7°	64.0°	57.5°	60.1°
Std. dev.	23.1°	21.5°	24.3°	23.1°

Table 5: 3D contact angle statistics for the air/water/glass-bead system. Each ROI is 1280 × 1280 × 640 voxels. N_{cp} represents the number of contact point used in the calculation.

Parameters	Coarse estimate			
	ROI 1	ROI 2	ROI 3	ROI combined
N_{cp}	12948	15040	13980	41968
Mean	60.7°	66.1°	60.9°	62.7°
Std. dev.	23.4°	22.6°	24.5°	23.6°
	Fine estimate			
N_{cp}	1771	2550	1755	6076
Mean	62.8°	66.5°	64.5°	64.8°
Std. dev.	22.0°	19.7°	20.0°	20.5°

respectively (Tables 4, 5). The reasonably close agreement observed between the 2D and 3D extractions for each estimate implies that the dimension of measurement does not change the result significantly. This probably happens because the error due to the interface orientation in 2D not being normal to the plane where contact angles are determined is random, so that for the large number of contact points its mean value is close to zero. The agreement between the 2D and 3D extractions further demonstrates that the 2D measurements can be utilized for a fast but coarse estimate of the mean *in situ* contact angle, but not the overall distribution as observed in the comparison of Fig. 13(a) and 14(a). Similarly, the difference in the mean extracted contact angle between both estimates are 5.5° and 2.1° for the 2D and 3D cases, respectively. This indicates that the coarse and fine estimates agree fairly well for both 2D and 3D extractions; the 3D calculations, howbeit, provide more reliable estimates. Furthermore, comparison between the 2D and 3D measurements shows that the standard deviations are similar for all estimates, with the 3D fine estimate having the least value.

Table 6: Comparisons between manual and automatic estimates. N_{cp} represents the number of contact point used in the calculation.

Parameter	manual	automatic
N_{cp}	68	68
Mean	65.2°	66.9°
Std. dev.	11.6°	14.3°

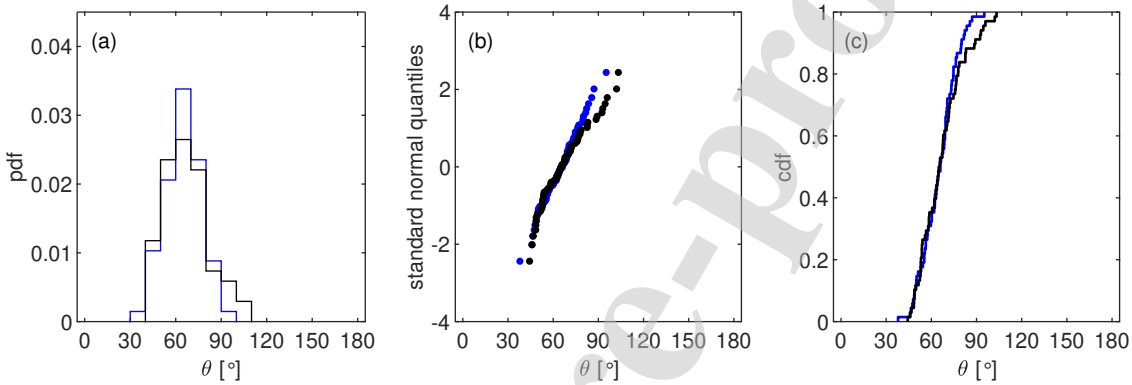

Fig. 15: The probability density function (a), standard normal quantiles (b), and cumulative distribution function (c) of manual (blue) versus automated 2D (Fine estimate) contact angle (black). Mean and standard deviation are reported in Table 6.

4.3.2. Comparison of manual versus automatic estimates

Manual contact angle estimates were obtained from segmented slices within a sub-volume (0.063 mm^3) of the image using our custom-made angle measurement Matlab script. Automatic contact angles of the 2D Fine estimate were also computed on a point-by-point basis from the same slices as those used for the manual estimates. Mean values and standard deviations for the two methods (Table 6) show a good agreement. The pdf, quantile, and cdf of both methods are shown in Fig. 15. The plots indicate that there is an overall consistency between the contact angle distributions from both estimates.

Furthermore, X-ray images showing examples of extracted contact angles of the air/water/glass system are presented in Fig. 16. Visual inspection suggests that the measurements reflects the actual contact angle formed at the three-phase contact point of each image.

4.3.3. Comparison of contact angle estimates from 2D planes

To investigate the effect of the 2D geometry of the packed column on the contact angle estimates, contact angles were extracted from the xy, zx, and yz slices of the 1.25 μm scan described in Section 4.2. The planes

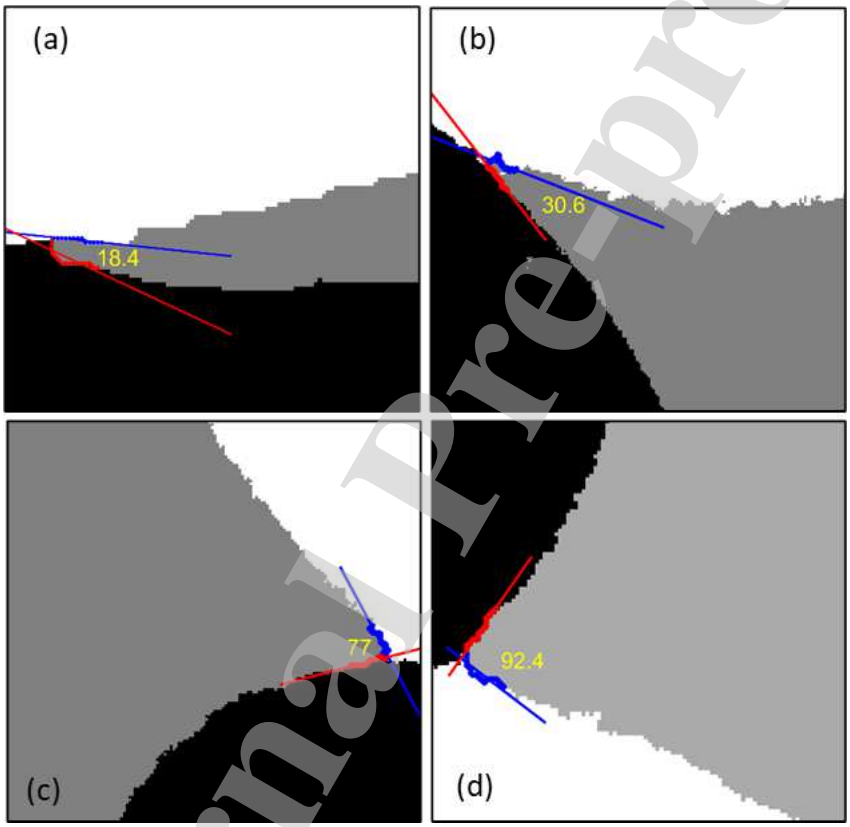

Fig. 16: 2D images of the 1.25 μm air/water/glass tomogram showing some measured contact angles of the 2D Fine estimate. Air, water, and glass are shown in black, grey and white, respectively.

Table 7: 2D contact angle statistics for the Fine estimates of the 10 μm and 1.25 μm scans. Each volume comprises $1000 \times 1000 \times 901$ and $1280 \times 1280 \times 1920$ voxels for the 10 μm and 1.25 μm scans, respectively. N_{cp} represents the number of contact point used in the calculation.

Parameters	10 μm	1.25 μm		
		xy	zx	yz
N_{cp}	301744	18289	17686	15338
Mean	86.9°	60.1°	53.3°	58.6°
Std. dev.	26.3°	23.1°	21.8°	25.5°

are defined by the right-hand Cartesian coordinate system as shown in Fig. 3. xy plane is normal to gravity and the principal flow direction during imbibition/drainage whereas other two planes are normal to xy and to each other. The pdf, quantile, and cdf of the xy (magenta) plane are presented in Fig. 17; superposed are the corresponding plots for the zx (black) and yz (blue) planes. The plot shows that the zx plane deviates slightly from the other two planes, which themselves are almost indistinguishable. The extracted contact angle statistics are presented in Table 7. Results showed that the xy-zx, xy-yz, and zx-yz planes differ by a mean and standard deviation of $6.8 \pm 1.3°$, $1.5 \pm 2.4°$, and $5.3 \pm 3.7°$, respectively, suggesting that the xy and yz planes are both very similar. The zx plane had the smallest mean contact angle, similar to results obtained by Dalton et al. [31] for manual computations of contact angle from the three plane orientations. Furthermore, comparisons between results in Tables 5 and 7 shows that the xy plane had a mean and standard deviation that are most comparable to the 3D estimates, thus suggesting that the plane which is normal to the flow direction should be the most suitable slice orientation for rapid estimation of the mean contact angle.

4.3.4. Limitations of the method

Segmentation can have a huge impact on the contact angle estimates as there are tendencies for artefacts to be introduced during the segmentation process [33–35]. However, a good segmentation result can be obtained with both the trainable WEKA and seeded watershed methods.

Resolution limits in the image acquisition can also impact the contact angle estimates. It is given that the algorithm will tend to overestimate contact angles as a result of the stair-wise representation of the surfaces (see Section 3). To illustrate the effect of resolution on the contact angle estimates, we extract *in situ* contact angles from the vertical tomograms of the 10 μm scan described in Section 4.2. The contact angle statistics of the 2D Fine estimate are reported in Table 7. Comparison of the results from both the 10 μm and 1.25 μm scans (Tables 7) shows that the number of contact points available for the calculation

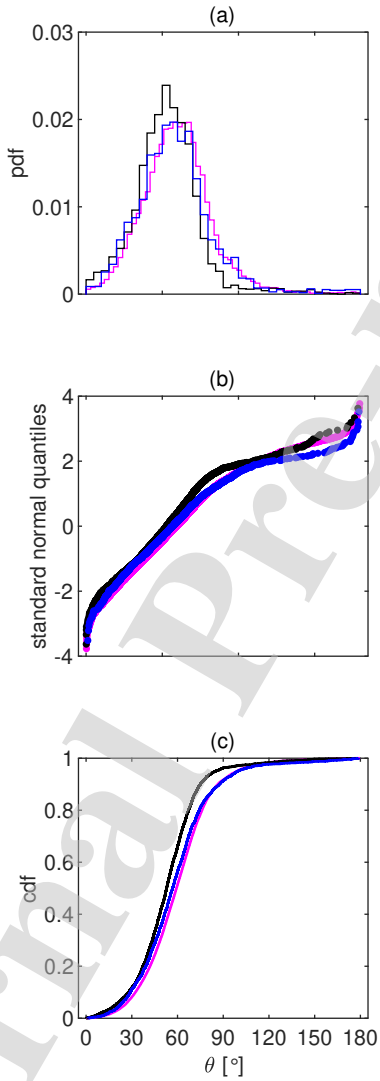

Fig. 17: The probability density function (a), standard normal quantiles (b), and cumulative distribution function (c) for contact angle estimates from xy (magenta), zx (black), and yz (blue) planes. Mean and standard deviations are reported in Table 7.

from the 10 μm scan is an order of magnitude larger than that from the 1.25 μm scan. However, the 10 μm scan is significantly larger in mean and standard deviation by a difference of $27 \pm 3°$, thereby demonstrating that the contact angle estimates are sensitive to image resolution.

5. Conclusions

We present an automatic algorithm for measuring *in situ* contact angles from both 2D and 3D pore space images. The algorithm is based on a fine estimate of contact angles from planes fit across the fluid/fluid and fluid/solid surfaces of two immiscible fluids in porous media. A coarse (intermediate) estimate is also obtained from the average normal vectors of both surfaces. The algorithm was validated over a range of resolutions for both 2D and 3D cases using synthetic images of circular/spherical non-wetting phase droplets in contact with a solid surface. The algorithm was then applied to air/water/glass system. Results show that:

(i) *in situ* contact angles span the full range of possible values, i.e., 0 to 180°, even within a uniform bed of spheres.

(ii) The mean and standard deviation of the contact angle is $65 \pm 21°$, indicating that the system is water-wet. This is significantly larger than bulk contact angles of $35 \pm 3°$, and demonstrates that bulk contact angles can dramatically underestimate *in situ* contact angle even in the simplest porous media.

(iii) The extracted contact angles are skewed towards their mean and are longer-tailed compared to a Gaussian distribution.

(iv) For a uniform packed bed of spheres at water-wet conditions, a ROI of $1280 \times 1280 \times 640$ voxels, containing an average of 1500 contact points, yields a representative contact angle distribution.

(v) Contact angles extracted from the vertical (i.e. xy) 2D slices have similar mean as the 3D contact angles, hence suggesting that the 2D algorithm, particularly when applied on the plane normal to the principal flow direction during drainage/imbibition, can be used for rapid estimation of the mean contact angle, but not the overall distribution.

Acknowledgements

This material contains work supported by an Aberdeen Formation Evaluation Society student bursary, a Society of Petrophysicist and Well-Log Analysts Foundation grant, and a Messel travel bursary from the Society of Chemical Industry. AI was supported by the University of Aberdeen School of Engineering

Elphinstone PhD studentship. The authors gratefully acknowledge Amer Alhammadi [33] for helpful suggestions on the segmentation and Kamaljit Singh for providing unpublished *in situ* contact angle measurements (Fig. 11a) for oil ganglion SSa. The authors thank the two anonymous reviewers for their comments.

References

[1] S. Y. Yang, G. J. Hirasaki, S. Basu, R. Vaidya, Mechanisms for contact angle hysteresis and advancing contact angles, Journal of Petroleum Science and Engineering 24 (2) (1999) 63–73.

[2] J. L. Dickson, G. Gupta, T. S. Horozov, B. P. Binks, K. P. Johnston, Wetting phenomena at the CO_2/water/glass interface, Langmuir 22 (5) (2006) 2161–2170.

[3] J. Shang, M. Flury, J. B. Harsh, R. L. Zollars, Comparison of different methods to measure contact angles of soil colloids, Journal of Colloid and Interface Science 328 (2) (2008) 299–307.

[4] D. Y. Kwok, T. Gietzelt, K. Grundke, H.-J. Jacobasch, A. W. Neumann, Contact angle measurements and contact angle interpretation. 1. contact angle measurements by axisymmetric drop shape analysis and a goniometer sessile drop technique, Langmuir 13 (1997) 2880–2894.

[5] D. Broseta, N. Tonnet, V. Shah, Are rocks still water-wet in the presence of dense CO_2 or H_2S?, Geofluids 12 (4) (2012) 280–294.

[6] D. N. Espinoza, J. C. Santamarina, Water-CO_2-mineral systems: interfacial tension, contact angle, and diffusion - implications to CO_2 geological storage, Water Resources Research 46 (7) (2010) 1–10.

[7] J. Drelich, J. D. Miller, R. J. Good, The effect of drop (bubble) size on advancing and receding contact angles for heterogeneous and rough solid surfaces as observed with sessile-drop and captive-bubble techniques, Journal of Colloid and Interface Science 179 (1) (1996) 37–50.

[8] P. Chiquet, J. Daridon, D. Broseta, S. Thibeau, CO_2/water interfacial tensions under pressure and temperature conditions of CO_2 geological storage, Energy Conversion and Management 48 (3) (2007) 736–744.

[9] W. G. Anderson, Wettability Literature Survey - part 2: Wettability measurement, Journal of Petroleum Technology 38 (12) (1986) 1246–1262.

[10] N. R. Morrow, The effects of surface roughness on contact angle with special reference to petroleum recovery, Journal of Canadian Petroleum Technology 14 (4) (1975) 42–53.

[11] N. R. Morrow, Wettability and its effect on oil recovery, Journal of Petroleum Technology 42 (12) (1990) 1476–1484.

[12] N. R. Wenzel, Resistance of solid surfaces to wetting by water, Industrial & Engineering Chemistry 28 (8) (1936) 988–994.

[13] J. Wan, Y. Kim, T. K. Tokunaga, Contact angle measurement ambiguity in supercritical CO_2-water-mineral systems: mica as an example, International Journal of Greenhouse Gas Control 31 (2014) 128–137.

[14] A. Islam, S. Chevalier, M. Sassi, Structural characterization and numerical simulations of flow properties of standard and reservoir carbonate rocks using micro-tomography, Computers and Geosciences 113 (2018) 14–22.

[15] S. Sleutel, V. Cnudde, B. Masschaele, J. Vlassenbroek, M. Dierick, L. V. Hoorebeke, P. Jacobs, S. D. Neve, Comparison of different nano- and micro-focus X-ray computed tomography set-ups for the visualization of the soil microstructure and soil organic matter, Computers & Geosciences 34 34 (2008) 931–938.

[16] S. M. Som, J. W. Hagadorn, W. A.Thelen, A. R. Gillespie, D. C. Catling, R. Buick, Quantitative discrimination between

geological materials with variable density contrast by high resolution X-ray computed tomography: An example using amygdule size-distribution in ancient lava flows, Computers & Geosciences 54 (2013) 231–238.

[17] M. Starnoni, D. Pokrajac, J. E. Neilson, Computation of fluid flow and pore-space properties estimation on micro-CT images of rock samples, Computers & Geosciences 106 (2017) 118–129.

[18] J. Titschack, D. Baum, K. Matsuyama, K. Boos, C. Färber, W. A. Kahl, K. Ehrig, D. Meinel, C. Soriano, S. R. Stock, Ambient occlusion - a powerful algorithm to segment shell and skeletal intrapores in computed tomography data, Computers and Geosciences 115 (2018) 75–87.

[19] D. Wildenschild, A. P. Sheppard, X-ray imaging and analysis techniques for quantifying pore-scale structure and processes in subsurface porous medium systems, Advances in Water Resources 51 (2013) 217–246.

[20] H. Menke, B. Bijeljic, M. Andrew, M. J. Blunt, Dynamic pore-scale imaging of reactive transport in heterogeneous carbonates at reservoir conditions, Energy Procedia 63 (2014) 5503–5511.

[21] J. G. Celauro, V. A. Torrealba, Z. T. Karpyn, K. A. Klise, S. A. McKenna, Pore-scale multiphase flow experiments in bead packs of variable wettability, Geofluids 14 (1) (2014) 95–105.

[22] S. Iglauer, A. Paluszny, C. H. Pentland, M. J. Blunt, Residual CO_2 imaged with X-ray micro-tomography, Geophysical Research Letters 38 (21) (2011) 1–6.

[23] Z. T. Karpyn, M. Piri, G. Singh, Experimental investigation of trapped oil clusters in a water-wet bead pack using X-ray microtomography, Water Resources Research 46 (4) (2010) 1–25.

[24] M. Shabaninejad, J. Middlelton, A. Fogden, Systematic pore-scale study of low salinity recovery from berea sandstone analyzed by micro-CT, Journal of Petroleum Science and Engineering 163 (2018) 283–294.

[25] M. Andrew, B. Bijeljic, M. J. Blunt, Pore-scale contact angle measurements at reservoir conditions using X-ray microtomography, Advances in Water Resources 68 (2014) 24–31.

[26] P. Lv, Y. Liu, Z. Wang, S. Liu, L. Jiang, J. Chen, In situ local contact angle measurement in a CO_2-brine-sand system using microfocused X-ray CT, Langmuir 33 (14) (2017) 3358–3366.

[27] M. Jafari, J. Jung, Direct measurement of static and dynamic contact angles using a random micromodel considering geological CO_2 sequestration, Sustainability 9 (12) (2017) 1–17.

[28] M. Khishvand, A. H. Alizadeh, M. Piri, In-situ characterization of wettability and pore-scale displacements during two- and three-phase flow in natural porous media, Advances in Water Resources 97 (2016) 279–298.

[29] M. Khishvand, A. H. Alizadeh, I. O. Kohshour, M. Piri, R. S. Prasad, In situ characterization of wettability alteration and displacement mechanisms governing recovery enhancement due to low-salinity waterflooding, Water Resources Research 53 (4) (2017) 4427–4443.

[30] J. Tudek, D. Crandall, S. Fuchs, C. J. Werth, A. J. Valocchi, Y. Chen, A. Goodman, In situ contact angle measurements of liquid CO_2, brine, and mount simon sandstone core using micro X-ray CT imaging, sessile drop, and lattice boltzmann modeling, Journal of Petroleum Science and Engineering 155 (2017) 3–10.

[31] L. E. Dalton, K. A. Klise, S. Fuchs, D. Crandall, A. Goodman, Methods to measure contact angles in scCO_2-brine-sandstone systems, Advances in Water Resources 122 (2018) 278–290.

[32] K. Singh, B. Branko, M. J. Blunt, Imaging of oil layers, curvature and contact angle in a mixed-wet and water-wet carbonate rock, Water Resources Research 52 (4) (2016) 1716–1728.

[33] A. Alhammadi, A. AlRatrout, K. Singh, B. Bijeljic, M. J. Blunt, In situ characterization of mixed-wettability in a reservoir rock at subsurface conditions, Scientific Reports 7 (10753) (2017) 1–9.

[34] K. A. Klise, D. Moriarty, H. Yoon, Z. T. Karpyn, Automated contact angle estimation for three-dimensional X-ray microtomography data, Advances in Water Resources 95 (2016) 152–160.

[35] A. Scanziani, K. Singh, M. J. Blunt, A. Guadagnini, Automatic method for estimation of in situ effective contact angle from X-ray micro tomography images of two-phase flow in porous media, Journal of Colloid and Interface Science 496 (2017) 51–59.

[36] A. AlRatrout, A. Q. Raeini, B. Bijeljic, M. J. Blunt, Automatic measurement of contact angle in pore-space images, Advances in Water Resources 109 (2017) 158–169.

[37] A. Scanziani, K. Singh, T. Bultreys, B. Bijeljic, M. J. Blunt, In situ characterization of immiscible three-phase flow at the pore scale for a water-wet carbonate rock, Advances in Water Resources 121 (2018) 446–455.

[38] A. AlRatrout, M. J. Blunt, B. Bijeljic, Spatial correlation of contact angle and curvature in pore-space images, Water Resources Research 54 (2018) 6133–6152.

[39] A. AlRatrout, M. J. Blunt, B. Bijeljic, Wettability in complex porous materials, the mixed-wet state, and its relationship to surface roughness, Proceedings of the National Academy of Sciences of the United States of America 115 (36) (2018) 8901–8906.

[40] K. Singh, M. Blunt, High resolution X-ray micro-tomography datasets for in-situ effective contact angle analysis in carbonate rocks, Digital Rocks Portal 10.17612/P7D95F (2018).

[41] Y. Tanino, M. Christensen, Imbibition capillary pressure and relative permeability of mixed-wet microporous rock: New insights from history matching, Transport in Porous Media 129 (1) (2019) 121–148.

[42] X. Li, X. Fan, S. Brandani, Difference in pore contact angle and the contact angle measured on a flat surface and in an open space, Chemical Engineering Science 117 (2014) 137–145.

[43] I. Arganda-Carreras, V. Kaynig, C. Rueden, K. W. Eliceiri, J. Schindelin, A. Cardona, H. S. Seung, Trainable weka segmentation: a machine learning tool for microscopy pixel classification, Bioimage informatics 33 (15) (2017) 2424–2426.

[44] S. Schluter, A. Sheppard, K. Brown, D. Wildenschild, Image processing of multiphase images obtained via X-ray micro-tomography: a review, Water Resources Research 50 (4) (2014) 3615–3639.

[45] J. M. Chambers, W. S. Cleveland, B. Kleiner, P. A. Tukey, Graphical methods for data analysis, Wadsworth International Group, Boston: Duxbury Press, 1983.

Highlights

- A simple algorithm for in situ contact angles in porous media has been developed.
- Algorithm can measure contact angle for any geometry of the fluid/fluid interface.
- Algorithm has been applied to packed glass spheres under air/water drainage.
- In situ contact angles are much larger than those measured on a flat substrate.

Declaration of interests

☒ The authors declare that they have no known competing financial interests or personal relationships that could have appeared to influence the work reported in this paper.

☐The authors declare the following financial interests/personal relationships which may be considered as potential competing interests: